

Dual-band Photonic Filters with Wide Tunable Range Using Chirped Sampled Gratings

SIMENG ZHU,* BOCHENG YUAN, WEIQING CHENG, YIZHE FAN, YIMING SUN, MOHANAD AL-RUBAIEE, JEHAN AKBAR, JOHN H. MARSH, LIANPING HOU

James Watt School of Engineering, University of Glasgow, Glasgow, G12 8QQ, U.K.

*Corresponding author: 2635935z@student.gla.ac.uk

We have developed a photonic filter featuring dual independently tunable passbands. Employing the reconstruction equivalent-chirp technique, we designed linearly chirped sampled Bragg gratings with two equivalent phase shifts positioned at $1/3$ and $2/3$ of the cavity, thus introducing two passbands in the $+1^{\text{st}}$ channel. Leveraging the significant thermo-optic effect of silicon, dual-band tuning is achieved via micro-heaters integrated on the chip surface. By tuning the injection currents ranging from 0 to 35 mA into the micro-heaters, the filter exhibits a wide range of dual-wavelength filtering performance, with the frequency interval between the two passbands adjustable from 37.2 GHz to 186.1 GHz.

With the ongoing expansion of 5G mobile communications, satellite communications, and Internet of Things (IoT) applications, the demand for multiband communication in wireless Radio Frequency (RF) systems is increasingly growing [1-2]. Photonic filters (PFs), as critical components in microwave photonics, are receiving significant attention due to their outstanding frequency selection, filtration performance, and dynamic tunability [2-4]. Stimulated Brillouin Scattering (SBS)-based PFs have become a popular research topic due to their high resolution and GHz-level tuning capability [5-6]. However, they require centimeter-scale waveguides [6] to generate only a single notch, and the local oscillator (LO) tone required for SBS must be generated through complex external intensity modulators and additional bandpass filters [5]. To meet the dynamic operational demands of multiband communications, the development of adjustable and reconfigurable multiband photonic filters is urgent. Recent studies have reported the design of various tunable dual-band filters, which can be implemented through several approaches. These include two cascaded microring resonators (MRR) with a tuning range of 6-17 GHz [7], electro-optic (EO) modulation-based distributed feedback Bragg-grating resonators (DFBR) with a -3 dB bandwidth of 24 GHz and a cavity length of 875 μm each [8], or using single resonator configurations such as equivalent phase-shift fiber Bragg grating (EPS-FBG) with a tuning range of only 7.4 GHz [9], the dual-arm Mach-Zehnder interferometer (MZI) with a tuning range of 1-18 GHz [10], and dual phase-shifted Bragg grating (PS-BG) with a tuning range of 113.4 GHz, though the passbands cannot be tuned

independently [11].

In this paper, we designed and fabricated a dual-bandpass filter based on silicon on insulator (SOI) platform, achieving independent tuning of two passbands on a single grating based on photonic integrated waveguide for the first time. The filtering section of the device consists of an equivalent chirped sampled grating (CSG) and two equivalent π phase shifts (EPS). The two equivalent phase shifts are designed to generate two passbands in the $+1^{\text{st}}$ channel. The equivalent chirp of the grating spatially separates the photon distributions of the two passbands, enabling independent tuning of the passband wavelengths. Meanwhile, this equivalent chirp is achieved by linearly modulating the micron-scale sampling period, which significantly reduces manufacturing difficulty compared to modulating the nanometer-scale seed grating period [12]. Two micro-heaters (MH) are respectively placed at the two EPSs locations. By utilizing the thermo-optic (TO) effect to change the phase magnitude of two EPSs, the central wavelength of the passbands can be adjusted.

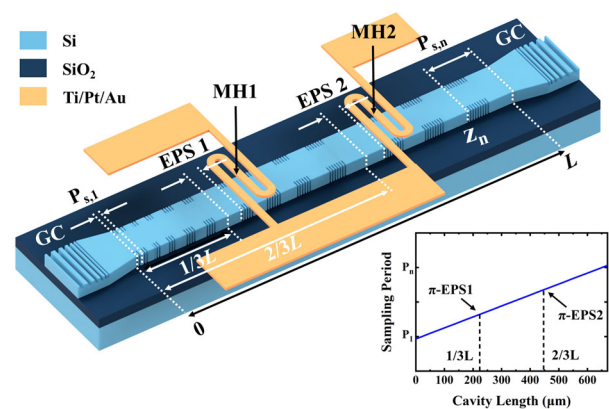


Fig. 1. Schematic of the CSG includes two π -equivalent phase shifts (π -EPSs), integrated input and output GCs, and two MHs positioned above the EPSs.

Compared to conventional MZI and MR, the device proposed here offers narrow passband frequencies and a large frequency tunable range unrestricted by the Free Spectral Range (FSR) [3], presenting unique advantages in wavelength selectivity and multiplexing capabilities, which are particularly critical for RF

manipulation. Simultaneously, our approach minimizes the quantity of resonators needed to process multiple signals, presenting a compact solution for photonic integrated circuits (PICs).

Fig. 1 is a schematic of the proposed device. The SOI wafer has a 220 nm top silicon layer and a 2 μm buried oxide (BOX) layer on a 675 μm thick silicon substrate. To generate two distinct passbands, two EPSs (EPS1 and EPS2) are strategically embedded at positions $1/3 L$ and $2/3 L$ along the CSG cavity's length (L).

By calculating the Fourier coefficients of the uniform sampled Bragg gratings, the coupling coefficient κ in +1st channel is $1/\pi$ times that of the uniform Bragg grating. Assuming there is a displacement ΔL inserted at position z of the cavity, then the refractive index modulation $\Delta n(z)$ is

$$\Delta n(z) = \frac{1}{2} \Delta n_0 S_{+1} e^{-i \frac{2\pi z}{\Lambda_0} - i \frac{2\pi z}{P_s} - i \frac{2\pi \Delta L}{P_s}} \quad (1)$$

where Δn_0 is the refractive index modulation amplitude of the seed grating, S_{+1} represents the Fourier expansion of the +1st channel, Λ_0 is the seed grating period, and P_s refers to the sampling period. Thus, when $2\pi \Delta L / P_s$ is equal to π , i.e., ΔL is equal to $P_s / 2$, this corresponds to the introduction of an equivalent π phase shift in the +1st channel [13].

The linear chirp sampling period distribution satisfies the following equation:

$$P_{s,n} = P_{s,1} + C \cdot z_n \quad (2)$$

where $P_{s,1}$ is the first sampling period, $P_{s,n}$ represents the sampling period at position of z_n . C refers to the chirp rate, defined as the ratio of the difference between the maximum and minimum sampling periods ($P_{s,n} - P_{s,1}$) to the cavity length L . In our device, the chirp rate C is set to nm/mm. By introducing a linear chirp to the sampled grating, the sampling periods at the two EPS locations differ, leading the two passbands to originate from different optical cavities, which enables independent tuning of the passbands.

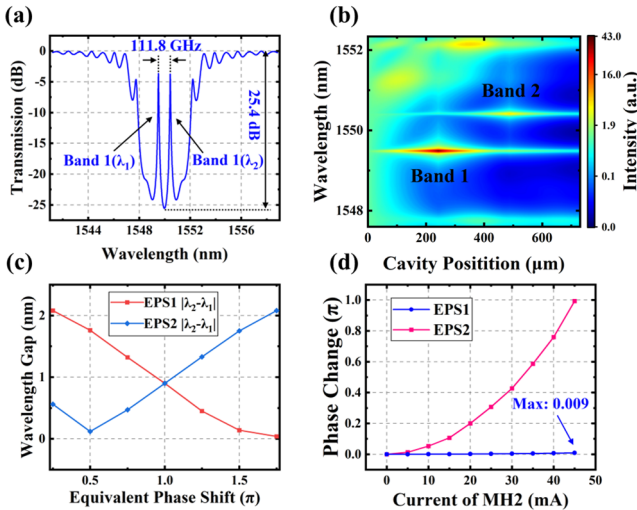


Fig. 2. Simulation results of (a) transmission spectrum of the two passbands; (b) photon distribution along the cavity; (c) wavelength drift versus phase shift value of EPS1 and EPS2, and (d) phase change value of EPS1 and EPS2 versus the inject current of MH2

Fig. 2(a) is the transmission spectrum of the proposed device calculated using the transmission matrix method (TMM) [14]. Two

narrow passbands (Q factor: 6.2×10^4), referred to as band 1 and band 2 (respective center wavelengths are λ_1 and λ_2) are clearly observed within the transmission stopband with a center wavelength of 1550 nm, aligning with the phase discontinuities caused by EPS1 and EPS2, respectively. The initial frequency spacing between band 1 and band 2 in the filter spectrum is 111.8 GHz, and the extinction ratio (ER) of the grating is 25.4 dB. The spatial photon distribution of the two passbands is shown in Fig. 2(b). After applying the chirp, the photons of λ_1 and λ_2 are concentrated at the two EPS locations, spatially separated, which reduces their interaction within the cavity. Therefore, when we modulate the value of a specific EPS, only one corresponding wavelength is adjusted, while the other remains unchanged. When an injection current is applied to the MH, the resistance wire is electrically heated due to the Joule effect, and the resulting heat is conducted downward through the deposited SiO_2 cladding (Thermal Conductivity: 1.1 W/mK at room temperature) [15]. Due to the substantial thermo-optic coefficient of silicon ($1.84 \times 10^{-4}/\text{K}$) [16], the refractive index of the buried waveguide changes with temperature, which is equivalent to a change in the phase of the EPS.

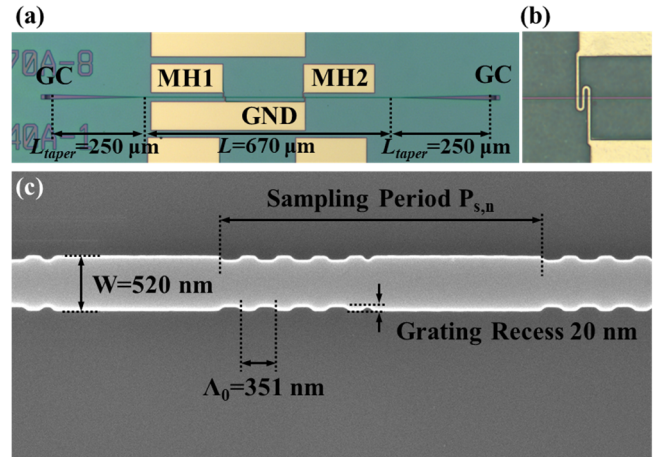


Fig. 3. (a) Optical microscope image of the PF device; (b) zoomed-in view of the MH; (c) scanning electron microscope (SEM) image of the CSG.

In Fig. 2(c), we calculated λ_1 and λ_2 under different values of EPS1 and EPS2 respectively while keeping the other EPS constant at π . The results show that increasing the phase shift of EPS1 causes a redshift in λ_1 , while λ_2 has a slight fluctuation of $\pm 0.06 \text{ nm}$ in the EPS range of 1π to 1.75π , resulting in a decrease in wavelength spacing from 111.8 GHz (initially unchanged EPS phase shift at π) to 5 GHz (at 1.75π). Similarly, increasing the phase shift of EPS2 while keeping EPS1 constant at π results in λ_1 remaining relatively stable ($\pm 0.02 \text{ nm}$) as EPS2 changes from 1π to 1.75π , while λ_2 shifts away from λ_1 , increasing the wavelength spacing to 259 GHz at 1.75π . This method achieves modulation of the filter passband spacing. As illustrated in Fig. 2(d), our calculations using COMSOL indicate that the thermal crosstalk is only 0.9% when a 45 mA drive current is applied exclusively to MH2. This indicates that the MH distribution in this device provides excellent thermal isolation, with the thermal effects on adjacent EPSs beyond 225 μm being negligible.

Fig. 3(a) is the optical microscope image of the fabricated device. Where the CSG section ($L=670 \mu\text{m}$) is at the center of the device and the two tapers ($L_{\text{taper}}=250 \mu\text{m}$) for connecting the CSG to the grating couplers (GC) are symmetrically integrated on both sides.

Highly localized MHs fabricated on the top cladding of the EPS positions enable independent tuning of EPSs by current injection. The MH consists of contact pads and heating resistance wires, with serpentine heating wires positioned directly above the two EPS regions, each with a width of $0.9\ \mu\text{m}$, a spacing of $0.8\ \mu\text{m}$, and a resistance of $10.7\ \Omega$ at 20°C as shown in Fig. 3(b). The MH spans a total waveguide length of $5.4\ \mu\text{m}$ and experiences an additional mode transmission loss of $3.5\ \text{dB/cm}$ when placed over the cladding. The extra transmission loss attributed to the two MHs is $6.6 \times 10^{-3}\ \text{dB}$. As depicted in Fig. 3(c), the side-wall gratings of the CSG are symmetrically arranged, featuring a uniform Bragg grating as the seed grating. This grating is defined by a period (Λ_0) of $351\ \text{nm}$, a grating recess of $20\ \text{nm}$, and a ridge waveguide width (W) of $520\ \text{nm}$. The CSG waveguide has an effective refractive index of 2.47 at a wavelength of $1550\ \text{nm}$.

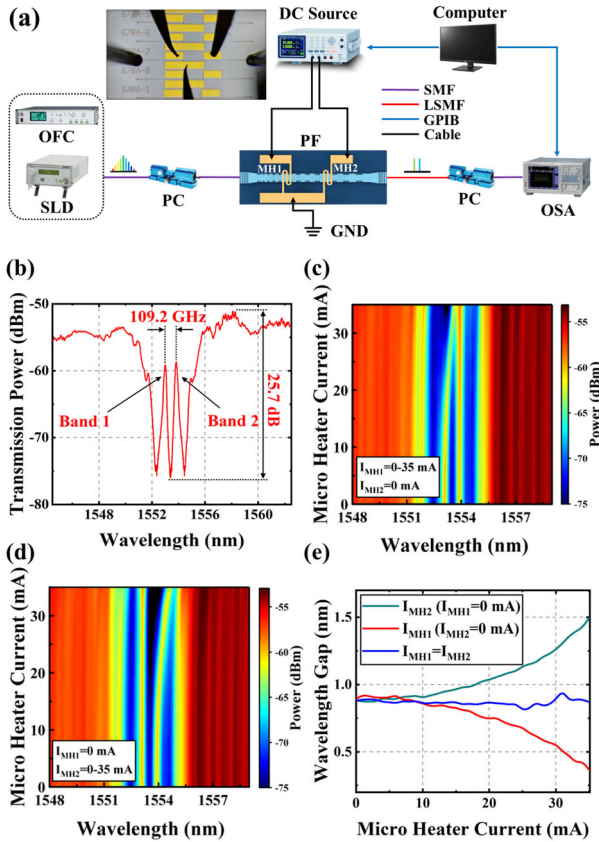


Fig. 4. (a) Schematic of the experiment setup; (b) transmission spectrum measured with no current applied to the MHs; (c) 2D optical spectra with only MH1 modulation; (d) 2D optical spectra with only MH2 modulation; (e) wavelength gap of the two passbands versus MH currents.

The grating samplings adhere to equation (2). The device comprises 215 complete sampling units distributed throughout its cavity, denoted by $n=215$. The chirp rate C is set at $100\ \text{nm/mm}$, with 1^{st} sampling period P_{s1} of $3.079\ \mu\text{m}$, aligning the $+1^{\text{st}}$ order channel near the wavelength of $1550\ \text{nm}$. The $66.9\ \text{nm}$ difference in sampling periods can be achieved with high precision using electron-beam lithography (EBL).

The device fabrication process begins by defining $210\text{-nanometer-high}$ Si ridge waveguides and side-wall gratings using EBL, and inductively coupled plasma (ICP) etching. The $10\ \text{nm}$ layer

of remaining Si prevents the removal of the underlying SiO_2 layer when using a hydrofluoric (HF) acid solution to remove the HSQ mask. Subsequently, employing polymethyl methacrylate (PMMA) photoresist and mask, a second round of EBL exposure and dry etching shapes $110\ \text{nm}$ high apodized GCs at the input and output ends of the CSG. Following this, a $300\ \text{nm}$ thick layer of SiO_2 is deposited on the wafer surface via plasma-enhanced chemical vapor deposition (PECVD) to create the buried waveguide. Surface flattening is achieved by spin-coating a $400\text{-nanometer-thick}$ layer of HSQ and annealing at 180°C . Finally, the MHs part, comprised of Ti ($20\ \text{nm}$), Pt ($160\ \text{nm}$), and Au ($50\ \text{nm}$), is defined by metal evaporation using lift-off technology with PMMA photoresist.

In Fig. 4(a), the experimental setup for device characterization at room temperature comprises a superluminescent diode (SLD) serving as the light source, with a central wavelength of $1551\ \text{nm}$ and a $3\ \text{dB}$ bandwidth of $30\ \text{nm}$. The single-mode fiber (SMF) is linked to the SLD, and a polarization controller (PC) directs the light onto the input GC surface. The output end utilizes a coated lensed single-mode fiber (LSMF) to couple the output light from the surface of the output GC and mitigate unwanted resonances originating from the Fabry-Pérot (FP) cavity between the fiber and the GC. The input and output SMFs are positioned directly above the GCs at an offset angle of 15° from the vertical direction. The output optical signal from the device is observed using an optical spectrum analyzer (OSA) with a resolution of bandwidth (RBW) of $0.06\ \text{nm}$. The output light wavelengths of the device can be tuned by adjusting the injection currents applied to the contact pads of MHs (I_{MH}).

Fig. 4(b) shows the transmission spectrum of the device with no injection currents applied to the MHs. The spectrum reveals dual passbands (Q factor: 1.48×10^4) within a $4\ \text{nm}$ range centered around the $1553.4\ \text{nm}$ stopband. Band 1 has a $-3\ \text{dB}$ bandwidth of $27\ \text{GHz}$ and a $-10\ \text{dB}$ bandwidth of $68\ \text{GHz}$, while band 2 features a $-3\ \text{dB}$ bandwidth of $28\ \text{GHz}$ and the same $-10\ \text{dB}$ bandwidth of $68\ \text{GHz}$. The frequency separation is $109.2\ \text{GHz}$, and the extinction ratio (ER) is $25.7\ \text{dB}$, closely matching the simulation results and demonstrating a balanced and consistent intensity distribution. The on-chip GC demonstrates a coupling loss of $10.2\ \text{dB}$ at the wavelength of $1550\ \text{nm}$. The $3.4\ \text{nm}$ redshift of the center wavelength compared to the simulation result may be due to etching the ridge waveguide height to $210\ \text{nm}$ instead of $220\ \text{nm}$ as in the simulation, which increases the effective index and, consequently, the center wavelength. The relatively lower Q factor compared to the simulation may be due to the limited RBW of OSA and fabrication imperfections, such as sidewall and surface roughness of the ridge waveguide, which introduce additional scattering losses, thereby reducing the Q factor. The effective grating coupling coefficient κ for the $+1^{\text{st}}$ channel is measured to be $102/\text{cm}$. Fig. 4(c) illustrates the transmission spectrum when only I_{MH1} is tuned from $0\ \text{mA}$ to $35\ \text{mA}$. During the scan of I_{MH1} from 0 to $35\ \text{mA}$, the TO effect of the EPS induces a redshift of band 1. The center wavelength of band 2 experiences a slight redshift of $0.012\ \text{nm}$ ($<\text{RBW}$) during the modulation of MH1, allowing for independent tuning of a single band. The separation frequency changes from $109.2\ \text{GHz}$ to $37.2\ \text{GHz}$. The consistent positioning of the stopband suggests precise alignment and geometric layout of the MHs, with minimal residual heat leakage. Similarly, as depicted in Fig. 4(d), independent modulation of band 2 can also be achieved by solely tuning I_{MH2} . When I_{MH2} is tuned from $0\ \text{mA}$ to $35\ \text{mA}$ while $I_{MH1}=0\ \text{mA}$, the separation frequency shifts from $109.2\ \text{GHz}$ to 186.1

GHz, while band 1 has a wavelength deviation of only 0.03 nm (<RBW). During this process, band 2 maintains its narrowband characteristics, with the -3 dB bandwidth increasing slightly from 28 GHz to 29.4 GHz. Furthermore, as shown in Fig. 4(e), analysis of the changes in the passband spacing during MH modulation from 0 to 35 mA reveals continuous modulation capability ranging from 37.2 GHz to 186.1 GHz, enabling dynamic tuning of the separation of the passbands. According to the simulation results in Fig. 2(c) and Fig. 2(d), the tuning wavelength gap can range up to 259 GHz if the MH wire is optimized to prevent breakage when a high injection current (>35 mA) is applied. Experiments on synchronous modulation of the dual passbands by tuning I_{MH1} and I_{MH2} from 0 mA to 35 mA simultaneously were also conducted, maintaining a relatively stable wavelength spacing and further confirming the independent tuning characteristic of the dual passbands.

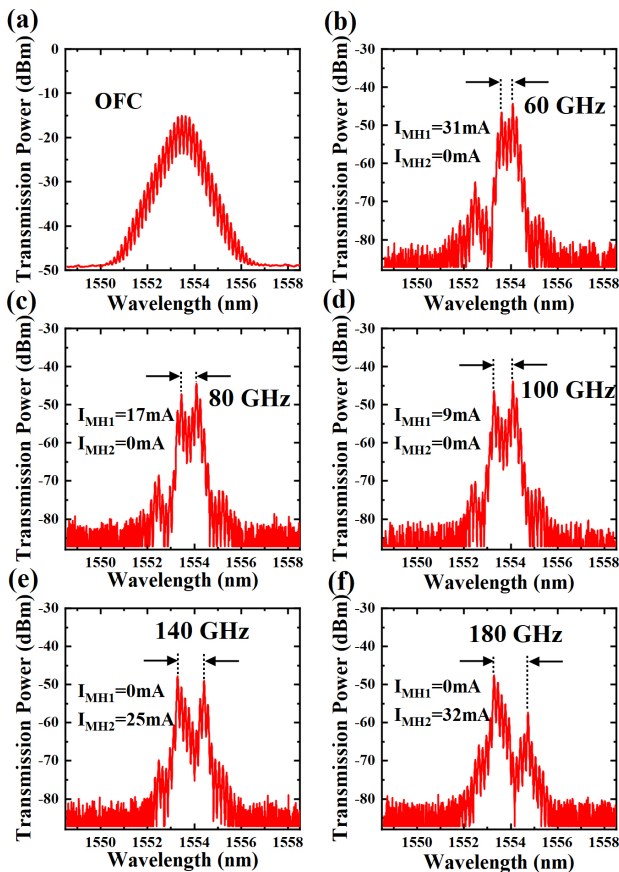


Fig. 5. Optical spectra of (a) unfiltered optical frequency comb, and with various filter settings with frequency separations of (b) 60 GHz, (c) 80 GHz, (d) 100 GHz, (e) 140 GHz, (f) 180 GHz.

We also employed an ultrafast optical clock (UOC) driven optical frequency comb (OFC) with a central wavelength of 1553.4 nm and a frequency interval of 20 GHz (Fig. 5(a)) to characterize our device. The output spectra shown in Fig. 5(b) to 5(f) were obtained by modulating the driving currents of MH1 and MH2, as depicted in the respective figures. An analysis of the optical frequency division (OFD) characteristics of the dual-wavelength PF revealed that the output spectra aligned with the trends observed using an SLD source shown in Fig. 4(e). Specifically, when only MH1 was modulated from low current to high current, band 1 initially approached band 2, decreasing the separation frequency of the PF.

Conversely, when only MH2 was modulated, band 2 moved away from band 1, increasing the separation frequency of the PF. The figures illustrate five distinct filtering configurations with separations of 60 GHz, 80 GHz, 100 GHz, 140 GHz, and 180 GHz, achieving a tunable filtering range from 60 GHz to 180 GHz, with the corresponding I_{MH1} and I_{MH2} . The 180 GHz configuration represents the maximum OFD spacing, limited by the 20 GHz OFC interval and the 27 GHz -3 dB channel bandwidth.

In summary, we present a dual-band independently tunable PF integrated on an SOI platform. Employing an SLD as the input source, the filter exhibits continuous frequency tuning capabilities spanning from 37.2 GHz to 186.1 GHz. Further characterization is conducted using an OFC with a 20 GHz interval, showcasing filtering capabilities from 60 GHz to 180 GHz. This dual-band tunable PF holds promise for applications in wireless communication, radar, and optical communication systems. Moreover, our technology can be extended for Terahertz (THz) photonic filter applications.

Funding. This work was supported by the U.K. Engineering and Physical Sciences Research Council (EP/R042578/1).

Acknowledgments. We would like to acknowledge the staff of the James Watt Nanofabrication Centre at the University of Glasgow for their help in fabricating the devices.

Disclosures. The authors declare no conflict of interest.

Data availability. Data underlying the results presented in this paper are not publicly available at this time but may be obtained from the authors upon reasonable request.

References

1. T. S. Rappaport, Y. Xing, G. R. MacCartney, *et al.*, IEEE Trans. Antennas Propag. **65**, 6213-6230 (2017).
2. M. Fok and J. Ge, Photonics. **4**, 45 (2017).
3. Y. Liu, A. Choudhary, D. Marpaung, *et al.*, Advances in Optics and Photonics. **12**, 485 (2020).
4. Z. Tao, Y. Tao, M. Jin, *et al.*, Photon. Res. **11**, 682-694 (2023).
5. S. Gertler, N. T. Otterstrom, M. Gehl, *et al.*, Nature Communications. **13**, (2022).
6. M. Garrett, Y. Liu, M. Merklein, *et al.*, Nature communications. **14**, (2023).
7. S. Song, S. X. Chew, X. Yi, *et al.*, J. Lightwave Technol. **36**, 4557-4564 (2018).
8. C. Porzi, A. Malacarne, A. Bigongiari, *et al.*, in the 49th European Conference on Optical Communication (ECOC 2023), 1-4 (2023).
9. L. Gao, J. Zhang, X. Chen, *et al.*, IEEE Trans. Microwave Theory Tech. **62**, 380-387 (2014).
10. Z. Jiao and J. Yao, J. Lightwave Technol. **38**, 5333-5338 (2020).
11. K. Abdelsalam, E. Ordouie, M. G. Vazimali, *et al.*, Opt. Lett. **46**, 2730-2733 (2021).
12. N. Ayotte, A. D. Simard, and S. LaRochelle, IEEE Photon. Technol. Lett. **27**, 755-758 (2015).
13. Y. Dai, X. Chen, D. Jiang, *et al.*, IEEE Photon. Technol. Lett. **16**, 2284-2286 (2004).
14. D. N. Maywar and G. P. Agrawal, IEEE J. Quantum Electron. **33**, 2029-2037 (1997).
15. D.-J. Yao, W.-C. Lai, and H.-C. Chien, in ASME 2008 First International Conference on Micro/Nanoscale Heat Transfer, Parts A and B (2008).
16. G. Cocorullo, F. G. Della Corte, and I. Rendina, Appl. Phys. Lett. **74**, 3338-3340 (1999).

References with title

1. T. S. Rappaport, Y. Xing, G. R. MacCartney, *et al.*, "Overview of millimeter wave communications for fifth-generation (5G) wireless networks— with a focus on propagation models," *IEEE Trans. Antennas Propag.* **65**, 6213-6230 (2017).
2. M. Fok and J. Ge, "Tunable Multiband Microwave Photonic Filters," *Photonics*. **4**, 45 (2017).
3. Y. Liu, A. Choudhary, D. Marpaung, and B. J. Eggleton, "Integrated microwave photonic filters," *Advances in Optics and Photonics*. **12**, 485 (2020).
4. Z. Tao, Y. Tao, M. Jin, *et al.*, "Highly reconfigurable silicon integrated microwave photonic filter towards next-generation wireless communication," *Photon. Res.* **11**, 682-694 (2023).
5. S. Gertler, N. T. Otterstrom, M. Gehl, A. L. Starbuck, C. M. Dallo, A. T. Pomerene, D. C. Trotter, A. L. Lentine, and P. T. Rakich, "Narrowband microwave-photonic notch filters using Brillouin-based signal transduction in silicon," *Nature Communications*. **13**, (2022).
6. M. Garrett, Y. Liu, M. Merklein, Cong Tinh Bui, Choon Kong Lai, D.-Y. Choi, S. J. Madden, A. Casas-Bedoya, and B. J. Eggleton, "Integrated microwave photonic notch filter using a heterogeneously integrated Brillouin and active-silicon photonic circuit," *Nature communications*. **14**, (2023).
7. S. Song, S. X. Chew, X. Yi, *et al.*, "Tunable single-passband microwave photonic filter based on integrated optical double notch filter," *J. Lightwave Technol.* **36**, 4557-4564 (2018).
8. C. Porzi, A. Malacarne, A. Bigongiari, *et al.*, "Silicon Photonics programmable millimeter-wave band RF synthesizer," in the 49th European Conference on Optical Communication (ECOC 2023), 1-4 (2023).
9. L. Gao, J. Zhang, X. Chen, *et al.*, "Microwave photonic filter with two independently tunable passbands using a phase modulator and an equivalent phase-shifted fiber Bragg grating," *IEEE Trans. Microwave Theory Tech.* **62**, 380-387 (2014).
10. Z. Jiao and J. Yao, "Passband-switchable and frequency-tunable dual-passband microwave photonic filter," *J. Lightwave Technol.* **38**, 5333-5338 (2020).
11. K. Abdelsalam, E. Ordouie, M. G. Vazimali, *et al.*, "Tunable dual-channel ultra-narrowband Bragg grating filter on thin-film lithium niobate," *Opt. Lett.* **46**, 2730-2733 (2021).
12. N. Ayotte, A. D. Simard, and S. LaRochelle, "Long integrated bragg gratings for Soi Wafer Metrology," *IEEE Photon. Technol. Lett.* **27**, 755-758 (2015).
13. Y. Dai, X. Chen, D. Jiang, *et al.*, "Equivalent phase shift in a fiber Bragg grating achieved by changing the sampling period," *IEEE Photon. Technol. Lett.* **16**, 2284-2286 (2004).
14. D. N. Maywar and G. P. Agrawal, "Transfer-matrix analysis of optical bistability in DFB semiconductor laser amplifiers with nonuniform gratings," *IEEE J. Quantum Electron.* **33**, 2029-2037 (1997).
15. D.-J. Yao, W.-C. Lai, and H.-C. Chien, "Temperature dependence of thermal conductivity for silicon dioxide," in *ASME 2008 First International Conference on Micro/Nanoscale Heat Transfer, Parts A and B* (2008), Paper No. MNHT2008-52052.
16. G. Cocorullo, F. G. Della Corte, and I. Rendina, "Temperature dependence of the thermo-optic coefficient in crystalline silicon between room temperature and 550 K at the wavelength of 1523 nm," *Appl. Phys. Lett.* **74**, 3338-3340 (1999).